JGR Planets

RESEARCH ARTICLE
10.1029/2019JE006335

# Crustal Porosity of Lunar Impact Basins

**D. Wahl[1], M. A. Wieczorek[2], K. Wünnemann[3,4], and J. Oberst[1,5]**

[1]Technische Universität Berlin, Department of Planetary Geodesy, Berlin, Germany, [2]Université Côte d'Azur, Observatoire de la Côte d'Azur, CNRS, Laboratoire Lagrange, Nice, France, [3]Museum für Naturkunde, Leibniz Institute for Evolution and Biodiversity Science, Berlin, Germany, [4]Freie Universität Berlin, Institut für Geologische Wissenschaften, Berlin, Germany, [5]German Aerospace Center (DLR), Department of Planetary Geodesy, Berlin, Germany

**Abstract** Lateral variations in bulk density and porosity of the upper lunar highland crust are mapped using a high-resolution Gravity Recovery and Interior Laboratory (GRAIL) gravity field model and Lunar Reconnaissance Orbiter (LRO) derived topography. With a higher spatial resolution gravity model than previous studies, we focus on individual impact basins with diameters greater than 200 km. The bulk density of the upper few kilometers of the lunar crust is estimated by minimizing the correlation between the topography and Bouguer gravity at short wavelengths that are unaffected by lithospheric flexure. Porosity is then derived using estimates of the grain density obtained from remote sensing data of the surface composition. The near surface crust in proximity to many large basins is found to exhibit distinct radial porosity signatures. Low porosities are found in the basin centers within the peak ring, whereas high porosities are identified near and just exterior to the main rim. The larger basins exhibit a more pronounced porosity signature than the smaller basins. Though the number of basins investigated in this study is limited, younger basins appear to be associated with the largest amplitude variations in porosity. For basins with increasing age the magnitude of the porosity variations decreases.

**Plain Language Summary** The gravity field surrounding an impact basin allows us to investigate the properties of the underlying crust and to better understand how craters form and evolve. In the center of the largest lunar craters, the impact basins, positive mass anomalies can be found that are caused by the excavation of crustal materials and the uplift of the mantle during formation. When using only the short wavelength portion of the gravity field, signals from these deeper regions are masked, and this allows us to estimate both the density and porosity of the upper crust. We investigated the crustal porosity of impact basins located in the lunar highlands, with diameters larger than 200 km. Many of these basins reveal similar porosity signatures, having low porosities in their center and high porosities near the crater rim. For the most pristine basins, the magnitude of the porosity variations increases with increasing basin size. Furthermore, the crustal porosity is influenced by the formation age of a basin, where the older basins have more muted signatures than younger basins.

**Key Points:**
- The bulk density and porosity of the upper highland crust are revisited using a high-resolution GRAIL gravity field model in combination with LOLA topography and independently estimated grain densities
- For many impact basins, porosity is reduced within their peak ring and increased near and just exterior to the main rim
- Large impact basins show a stronger pronounced porosity signature than smaller basins, and old impact basins reveal a muted porosity signature compared to younger basins

**Supporting Information:**
- Supporting Information S1
- Figure S1
- Figure S2
- Figure S3

**Correspondence to:**
D. Wahl,
daniel.wahl@tu-berlin.de

**Citation:**
Wahl, D., Wieczorek, M. A., Wünnemann, K., & Oberst, J. (2020). Crustal porosity of lunar impact basins. *Journal of Geophysical Research: Planets*, *125*, e2019JE006335. https://doi.org/10.1029/2019JE006335

Received 18 DEC 2019
Accepted 20 FEB 2020
Accepted article online 8 APR 2020

©2020. The Authors.
This is an open access article under the terms of the Creative Commons Attribution License, which permits use, distribution and reproduction in any medium, provided the original work is properly cited.

## 1. Introduction

High resolution data from the Gravity Recovery and Interior Laboratory (GRAIL) mission (Zuber et al., 2013a) allowed to investigate physical characteristics of the lunar interior. In combination with topography data, variations in bulk density of the lunar crust can be investigated (e.g., Besserer et al., 2014; Wieczorek et al., 2013), and when compared with independent knowledge of mineral grain densities based on remote sensing data, the porosity of crustal materials can be estimated. The main result of these studies is that the crust of the Moon exhibits high porosities, between about 4% and 21%, with an average of about 12%. While the interiors of many impact basins were found to have lower porosities, the two youngest and largest basins on the Moon, Moscoviense and Orientale, show particular high porosities in their surroundings (Wieczorek et al., 2013). Later work by Besserer et al. (2014) confirmed the high crustal porosities and placed constraints on how porosity decreases with depth below the surface.

The porosity of lunar impact craters was investigated by Soderblom et al. (2015) by analyzing their Bouguer gravity signatures. In order to avoid the contribution of the gravity signal caused by the uplift of mantle material (e.g., Melosh et al., 2013; Wieczorek & Phillips, 1998), their study was restricted to complex craters with

diameters smaller than 200 km. It was determined that preimpact porosity of the target material (estimated from the regional value far from the crater) controls the magnitude of the final Bouguer gravity anomaly. Impacts in targets with initially low porosity were found to result in a negative Bouguer anomaly, which they interpreted as being caused by the fragmentation of the underlying target rock. In contrast, impacts in target materials with high preimpact porosity result in positive Bouguer anomalies, which they attributed to compaction of the target rock leading to a reduced porosity.

Similar effects were found based on numerical simulations of impact crater formation, suggesting a major influence of the preimpact porosity on the final outcome. Milbury et al. (2015) simulated the formation of complex craters using the iSALE shock physics code (Collins et al., 2004; Wünnemann et al., 2006) and investigated the resulting crater porosity by analyzing the computed Bouguer gravity. While preimpact target porosities up to a maximum of 7% result in negative Bouguer anomalies (indicating higher postimpact porosities), initial porosities greater than 7% result in positive Bouguer anomalies (indicating lower postimpact porosities). In target materials with high preimpact porosity, the impact induced shock wave crushes out preexisting fractures and compresses the material (Wünnemann et al., 2006), causing a reduction of porosity (Milbury et al., 2015). At further distances, the preexisting porosity remains intact (Milbury et al., 2015), caused by a more efficient decay of the pressure wave in porous targets (Love et al., 1993). In contrast, for target material with a low preimpact porosiy, the energy is transported more efficiently, causing fracturing of rocks also in larger distance to the point of impact.

Examples from Earth show that regions of high porosity are to be expected within and surrounding impact basins. Rocks obtained from the central peak region of the Chicxulub impact structure in Mexico show strong fracturing. Analysis of the drill core samples revealed an average porosity of 11.5% for depths between 850 and 1250 m below the surface, whereas porosities as high as 20% were found in the uppermost portion of the drill core between 750 and 850 m depth (Rae et al., 2019). The high porosity is primarily caused by intragranular microfracturing, induced by the impact generated shock wave. The occurrence of cataclasites in the samples, having a high porosity but being small in volume, has only a minor contribution on the overall porosity of the rocks. Another well studied impact structure on Earth is the Ries crater in Germany. From the bulk densities of rock samples obtained from two drill cores, Förstner (1967) estimated the related porosity. The drill core in Wörnitzostheim, located between the inner ring and the outer crater rim, revealed a mean porosity of about 28% (at depths between 37 and 74 m), while the drill core taken in Deiningen, located close to the inner ring, shows porosities of up to 34% at depths between 311 and 350 m. Many terrestrial impact craters (including Chicxulub and Ries) show prominent negative Bouguer gravity signatures that are a result of impact induced porosity (e.g., Pilkington & Grieve, 1992; Pohl et al., 1977; Rae et al., 2019).

Samples from the Apollo program, as well as lunar meteorites, have been used to study the porosity of lunar rocks. For feldspathic material associated with the lunar highlands, Kiefer et al. (2012) found porosities between 2% and 20%. Impact breccias revealed the highest porosities of about 20%, while the feldspathic lunar meteorites hold the lowest porosities with values between 2% and 11.5%. Their results are consistent with those reported by Wieczorek et al. (2013), who studied 24 feldspathic Apollo samples and meteorites, finding porosities between 1% and 20%, with an average of 8.6% $\pm$ 5.3%. While considerations limited to Apollo samples collected at the surface might not capture the full range of all possible porosity characteristics, porosities of lunar meteorites may be biased to lower values due to the processes associated with ejection from the lunar surface and entry in Earth's atmosphere (Warren, 2001).

Since the first GRAIL investigations regarding crustal porosity, improved models of the Moon's gravity field have been derived with higher spatial resolutions and accuracies. The 420 degree and order model of Zuber et al. (2013a) was employed by Wieczorek et al. (2013), whereas in the later work of Besserer et al. (2014) the 900 degree and order model of Lemoine et al. (2014) was used. In the present work, we made use of the most recent gravity model of Park et al. (2015), which is developed to spherical harmonic degree and order 1500. The higher resolution of this model allows a detailed investigation of the porosity structure of individual impact basins on the Moon that was not possible in previous studies. Our approach to estimate the crustal density and porosity follows the method used by Wieczorek et al. (2013). By minimizing the correlation between the surface topography and the Bouguer gravity (using only the short wavelength signal that is unaffected by lithospheric flexure), bulk density variations of the highland crust were determined. In combination with independent knowledge of grain densities of the upper crust, the porosity of the upper crust was then calculated. With our derived maps we are able to study how the porosity variations are related

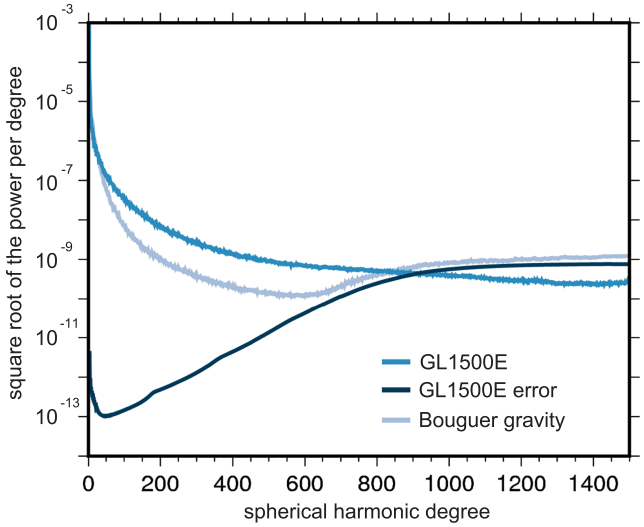


**Figure 1.** Power spectrum of the Gravity Recovery and Interior Laboratory (GRAIL) gravity field model GL1500E (Park et al., 2015), the related error spectrum, and the power of the Bouguer gravity (computed using a crustal density of 2,550 kg $m^{-3}$).

to the structure of the basin and also to quantify how the magnitude of the porosity signature varies with crater size and age.

In section 2, we describe how the new bulk density and porosity maps used in this study were constructed. In section 3.1, we present the global characteristics of the density and porosity model, and in section 3.2, we then systematically investigate the porosity signatures of large impact basins in the lunar highlands with diameters larger than 200 km. Finally, in section 4, we discuss several aspects related to the porosity signatures of the investigated impact basins, including how they are related to basin size and age.

## 2. Data and Methods

As a result of the GRAIL mission, the gravity field of the Moon is known with unprecedented accuracy and resolution. We made use of the most recent gravity field model GL1500E (Konopliv et al., 2014; Park et al., 2015) provided as spherical harmonic coefficients developed to degree and order 1500 (which corresponds to a spatial resolution of about 3.6 km). The effective resolution of the model, however, is highly dependent on the coverage of the low altitude data obtained at the end of the mission. To account for this variability in spatial resolution, we truncate the spherical harmonic coefficients at a maximum degree that is globally well resolved by the model. As shown in Figure 1, the power spectra of the gravity field and their related errors intersect at about degree 900, indicating that beyond this degree the global coefficients are poorly resolved.

A different indicator of the model's resolution comes from the spectrum of the Bouguer gravity. The Bouguer gravity represents the signal that remains after removing the expected signal of the surface topography from the free-air gravity (here using a crustal density of 2,550 kg $m^{-3}$). The power of this signal decreases until about degree 700, at which point the power begins to increase. Beyond this degree, the power of the Bouguer gravity is very similar to the error spectrum of the gravity field, and we interpret the increase in power beyond degree 700 as noise in the global spherical harmonic coefficients. We note that Wieczorek et al. (2013) truncated the gravity model at degree 310, whereas Besserer et al. (2014) truncated the field at degree 550. Thus, in comparison to Wieczorek et al. (2013), our derived density and porosity maps should have a resolution that is better by a factor of about two.

The topography model was derived from measurements made by the Lunar Orbiter Laser Altimeter (LOLA Smith et al., 2017). We employed the model LOLA2600p of Wieczorek (2015) which is a spherical harmonic expansion of the gridded data products archived on the NASA Planetary Data System. To match the resolution of the gravity field, we truncated the spherical harmonic series of the topographic model to the same degree and order as the gravity model. We note that both the topography and gravity field are given in the same principle axis reference frame (NASA, 2008).

We estimated the bulk density of the upper crust using techniques developed by Wieczorek et al. (2013), which were later elaborated by Wahl and Oberst (2019). In the approach, the Bouguer gravity is first determined by removing the gravitational signal of the surface topography from the observed gravity (both downward continued to the mean planetary radius). If all gravity anomalies were the result of surface topography, the Bouguer gravity would be zero if the correct density was chosen. Introducing an incorrect density value, the Bouguer gravity would be nonzero and show a correlation with the topography. The density can thus be determined, by ensuring that the correlation between Bouguer gravity and topography is as small as possible. The correlation between the two fields was computed locally, using data collected on a grid within a circle placed on the surface, and calculating the correlation coefficient we ensured that each point was weighted by its corresponding surface area. Before computing grids of the Bouguer gravity and topography, we first filtered out the longest wavelengths that could be influenced by lithospheric flexure. In particular, Wieczorek et al. (2013) showed that for degrees larger than 150, the gravitational signal resulting from the deflection of the crust-mantle interface is exceedingly small, regardless of what value is assumed for the lithospheric thickness. We accordingly set the spherical harmonic coefficients of these fields to zero for all degrees less than 150.

As described further in Wahl and Oberst (2019) we quantify the local variability of the bulk density based on the variance of the density estimates about a given analysis point. For this, we simply calculated the standard deviation of each point in relation to the neighboring values. Areas covered with mare were not considered in our study given that the density structure of the crust in these regions is complex, with dense basalts overlying less dense highland materials (Gong et al., 2016). In order to prevent dense mare basalts from biasing the results, we rejected estimated bulk densities where more than 2.5% of mare were present in the analysis region. All spherical harmonic analyses were performed using the freely available python-based pyshtools software package (Wieczorek & Meschede, 2018), and we make use of perceptually uniform colormaps generated by Crameri (2018).

After obtaining the bulk density, the porosity can be estimated if the grain density is known independently. Huang and Wieczorek (2012) showed that the grain density of common lunar rocks has a linear dependence on both FeO and $TiO_2$ abundances. In fact, the uncertainty in this dependence ($\pm 64$ kg m$^{-3}$; Huang & Wieczorek, 2012) is comparable to the uncertainty of our bulk density estimates ($\pm 21$ kg m$^{-3}$). Using the grain density map of Huang and Wieczorek (2012), for each analysis region we determine the average grain density and then calculate the porosity using the relation

$$\phi = 1 - \frac{\rho_{bulk}}{\rho_{grain}} \quad . \tag{1}$$

Finally, we note that the bulk density and porosity obtained in this study are representative of the upper few kilometers of the crust. In particular, for each analysis region, the density is representative of the material located between the highest and lowest elevations, and for most regions this is approximately 4 km. For any location considered in our analysis, we expect the crust to be thinner than a few kilometers. Besserer et al. (2014) showed that the porosity is expected to decrease with depth but that some porosity would still be present at the base of the crust.

## 3. Bulk Density and Porosity of the Upper Crust

### 3.1. Global Results

Following the methods described above, we produced a global map of the bulk density of the upper crust of the Moon, which is shown in Figure 2. Mare areas (Nelson et al., 2014) are outlined with thin black lines, and impact basins with diameters greater than 200 km (Neumann et al., 2015) are delineated by solid black circles. Analyses were performed on an equal area grid with a spacing of 0.75°, and bulk density analyses were carried out using the gravity and topography data within circles with a radius of 3° (about 90 km at the equator). The spatial resolution was chosen based on tradeoffs between the variance of the global maps, the uncertainties of the analyses, and expectations based on the maximum and minimum densities (and porosities). Our analyses thus have a spatial resolution that is two times better than in the initial study of Wieczorek et al. (2013), which is to be expected, given that the maximum spherical harmonic degree they employed (310) is about half of the value used here (700). Regardless, we note that none of our conclusions presented here are sensitive to changes in the radius of the analysis regions from 1.5° to 4.5° (corresponding to diameters of 90 and 272 km, respectively).

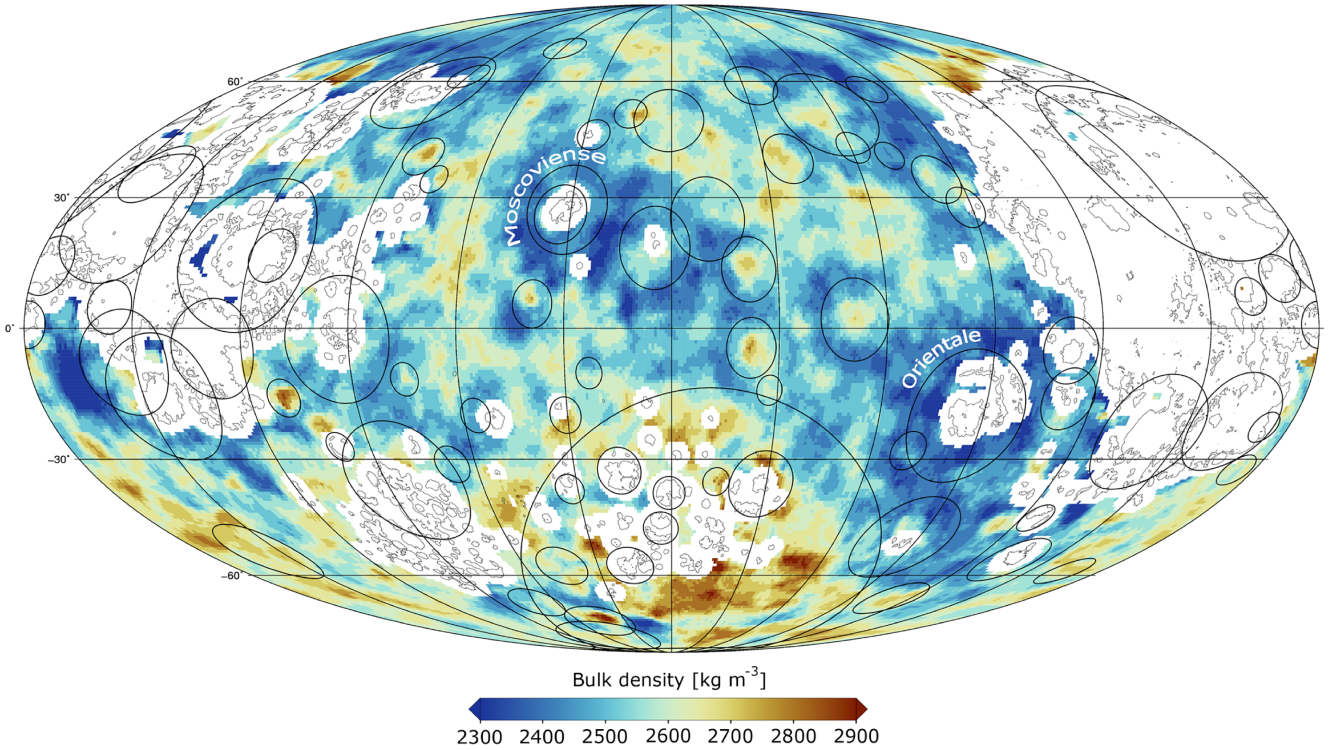


**Figure 2.** Bulk density of the upper crust. The map is shown using a Mollweide equal area projection, centered over the lunar farside at 180° E, 0° N. Impact basin main rims with diameters larger than 200 km are outlined by black circles and the mare, which were not considered in our study, are outlined with thin black lines. Regions, where analyses were not performed are shown as white. Each bulk density plotted in this map represents an average within a circle with a radius of 3° latitude, corresponding to a diameter of 180 km. The mare basalt map is taken from Nelson et al. (2014).

Averaging the local bulk densities in Figure 2, we compute a mean bulk density of the highland crust of 2,536 ± 21 kg m$^{-3}$. This value is consistent within uncertainties to the value of 2,550 ± 18 kg m$^{-3}$ from Wieczorek et al. (2013). The density is seen to vary from values as low as 2,300 kg m$^{-3}$ to as high as 2,900 kg m$^{-3}$. The bulk densities are also seen to be higher within the farside South Pole-Aitken basin (~2,700 kg m$^{-3}$) than in the surrounding highlands (~2,500 kg m$^{-3}$). The Orientale and Moscoviense basins are associated with prominent density lows exterior to their peak rings. Furthermore, several of the smaller farside basins, that do not possess interior mare, are seen to have slightly higher densities than their surroundings.

The porosity of the upper crustal materials was computed using the grain densities from Huang and Wieczorek (2012) and is plotted in Figure 3. The porosity in the lunar highland crust varies from about 3% to 24%, with an average of 13%, similar to the values obtained in Wieczorek et al. (2013). This map has several features in common with that of Figure 2. As examples, the density lows associated with the regions surrounding Orientale and Moscoviense basins are associated with enhanced porosities. Furthermore, the interiors of small basins with no mare fill correspond to porosity lows.

### 3.2. Porosity Signatures of Impact Basins

We next analyzed the porosity signatures of individual impact basins, making use of the basin catalog of Neumann et al. (2015). Several impact structures that are completely or largely covered by mare basalts were excluded from our investigation, given that their density structure is poorly constrained. These included many prominent basins on the nearside (such as Imbrium, Serentitatis, Crisium, Nectaris, and Humorum) as well as most of the basins located in the South Pole-Aitken (SPA) basin (such as Apollo). Some basins situated in the lunar highlands also show bulk density and porosity gaps due to the presence of mare basalts, but these gaps are mostly limited to the inner most portion of the basin and make up a very small portion of the data used in generating an azimuthally averaged radial porosity profile. In the end, we investigated 40 basins located in the lunar highlands with diameters greater than 200 km. For each basin, we created azimuthally averaged plots of porosity as a function of distance from the basin center, extending to 3 crater radii. For each point, we also computed the standard deviation, which is the measure of the natural variability of any

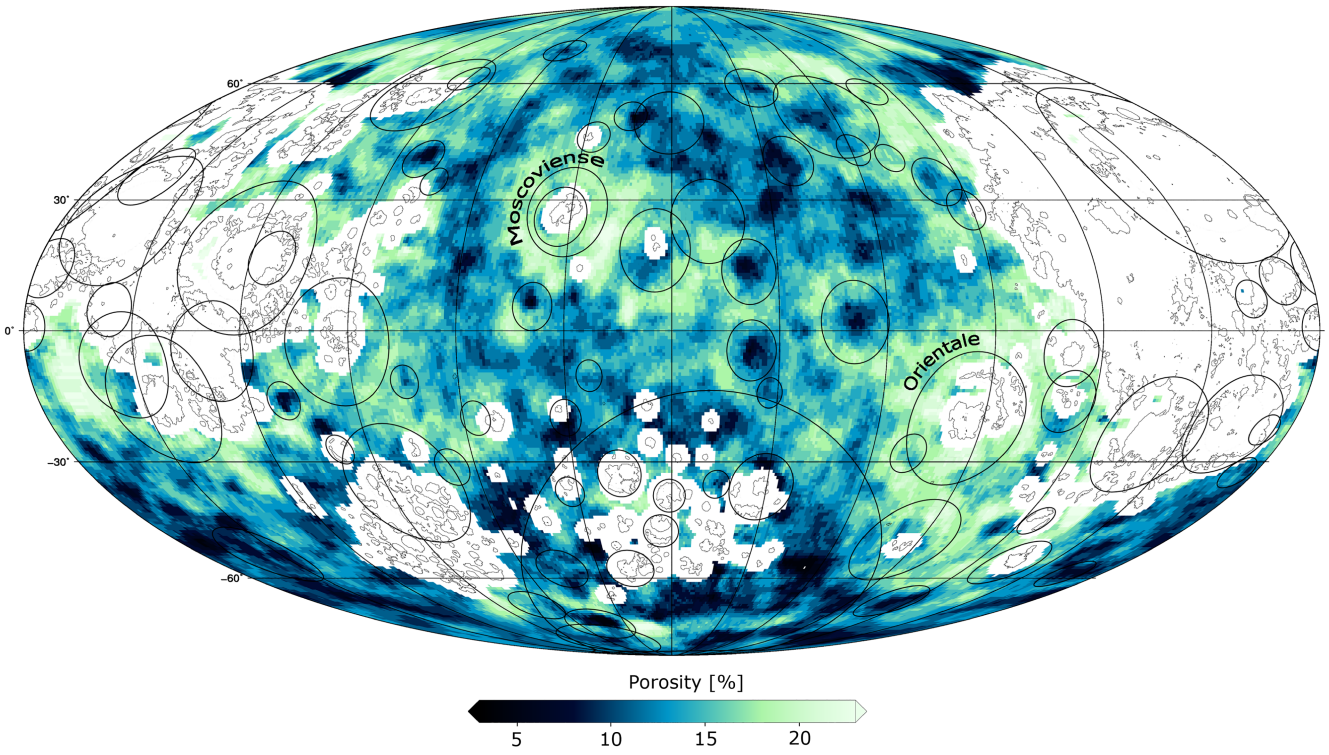


**Figure 3.** Porosity of the upper crust. Image format is the same as in Figure 2.

given point with respect to the mean value. To aide in comparing the porosity profiles of the various basins, we normalized the radial distances by the main rim diameter of each basin.

While some basins show no clear pattern in their radial porosity profiles, others exhibit a distinct signature. In Figure 4 we investigate two representative basins, the large 571 km diameter Hertzsprung basin (left) and the highly degraded basin TOPO-22 (right). The upper image shows a shaded-relief map of the basin, the middle panel shows our derived porosities in map form, and the lower image plots the azimuthally averaged porosity as a function of distance from the basin center. The main rim is marked as a solid, thick line at the distance of 1 crater radius, and the peak ring and inner depression (when present) are shown as dashed and dotted lines, respectively. Porosity profiles are normalized in distance by the main crater rim and the absolute distances from the basin center are shown on the upper axis.

For the Hertzsprung basin, the porosity signature is approximately concentric about the basin center. Regionally low porosities of 6% are found in the center of the basin, while just exterior to the main rim the porosity reaches its maximum value of about 15%. For this basin, the density contrast between the minimum and maximum values is 9% and we note that the lowest porosities are found interior to the peak ring, which has a diameter of about half of the main rim. Furthermore, this basin also possesses an inner depression that lies interior the peak ring, and the lowest porosities are closely correlated with the inner depression. In contrast, the slightly smaller, but highly degraded basin named TOPO-22 (Figure 4) shows a less distinctive and muted signature. The local minimum of 9% is found within the peak ring, and exterior to the main rim the porosity is quite variable and affected by multiple younger impact structures. The maximum porosity corresponds to the regional value far from the basin rim of about 14%. Consequently, TOPO-22 only possesses a modest porosity contrast of at most 5%. The porosity contrast between the basin center and the main rim is substantially lower at about 3%.

Azimuthally averaged porosity profiles of basins that have distinct porosity signatures are shown in Figure 5. A striking feature that can be observed for all basins presented in this figure is that the local minimum is always situated in the basin center inside the peak ring (if one exists). For many peak ring and mulitiring basins, the porosity abruptly increases interior of the peak ring (such as Birkhoff), whereas for others, the porosity continually increases interior of the main rim (such as Dirichlet-Jackson). The majority of these

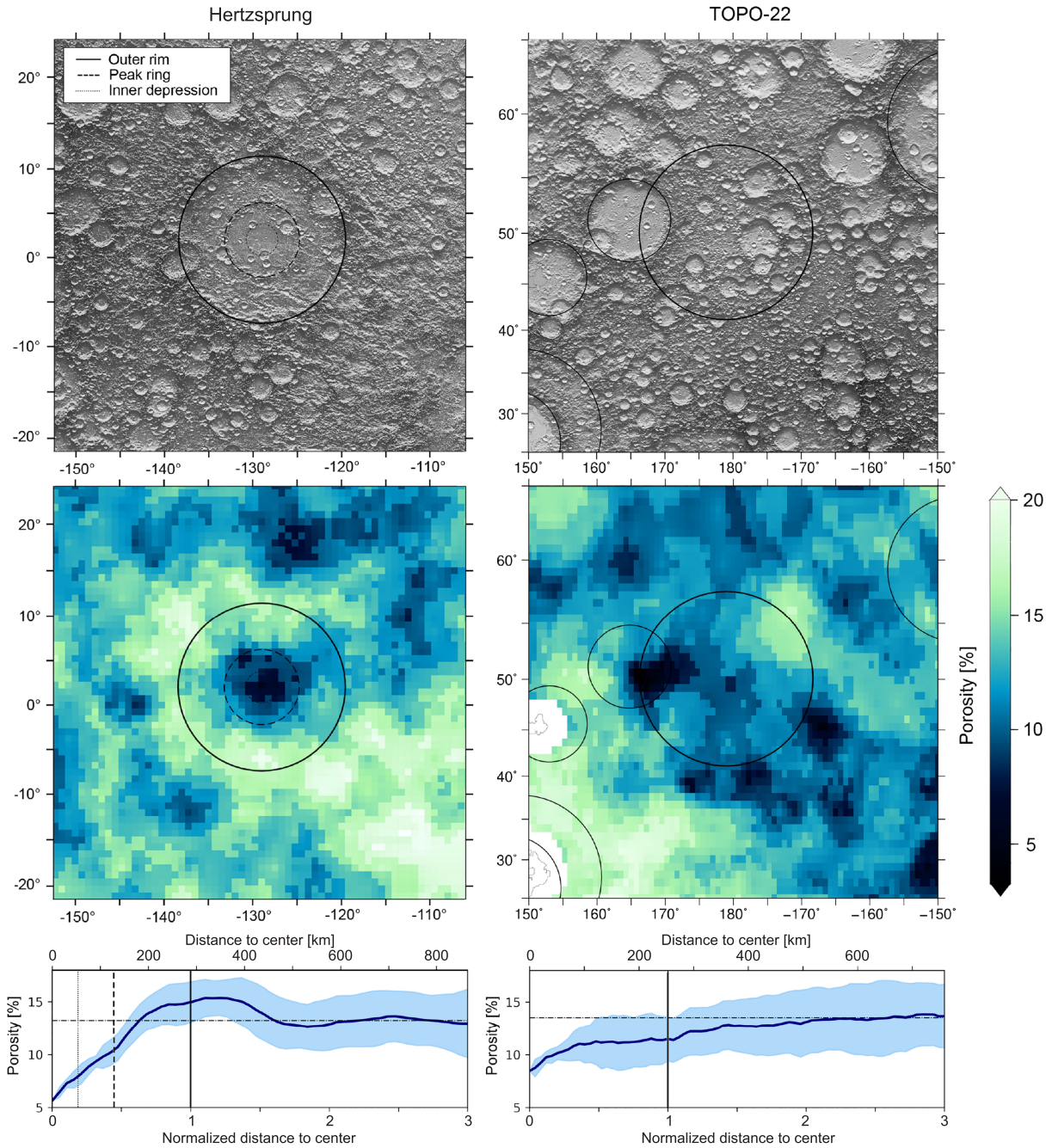


**Figure 4.** Porosity signatures of the Hertzsprung (left) and degraded TOPO-22 (right) impact basins. Plotted are shaded-relief maps (top), porosity maps (middle), and azimuthally averaged porosity profiles with associated standard deviations (bottom). In each image, basin ring diameters from Neumann et al. (2015) are plotted: main rim (solid), peak ring (dashed), and inner depression (dotted). Mare basalts (when present) are outlined in thin lines, and analysis regions that were excluded as a result of the mare basalts are plotted in white. Maps are shown in a Mercator projection. The distances given on the lower axis of the porosity profiles are normalized to the main rim radius, and the upper axis provides absolute distances. The horizontal dash-dotted line denotes the ambient porosity, which is the average porosity between 2 and 3 main rim radii from the basin center.

basins also show higher porosities than the regional average, extending from the peak ring (at ~0.5 crater radii) to beyond the main crater rim at about 1.5–2 crater radii. In the supporting information, Figure S1, we show basins without any distinct porosity signature and in Figure S2 basins where porosity measurements in their interiors are lacking due to the presence of mare basalt.

The most striking basins in a global context (Figure 3) are Moscoviense and Orientale, which are two of the largest and also youngest basins located in the lunar highlands. Moscoviense is a 640 km diameter basin that

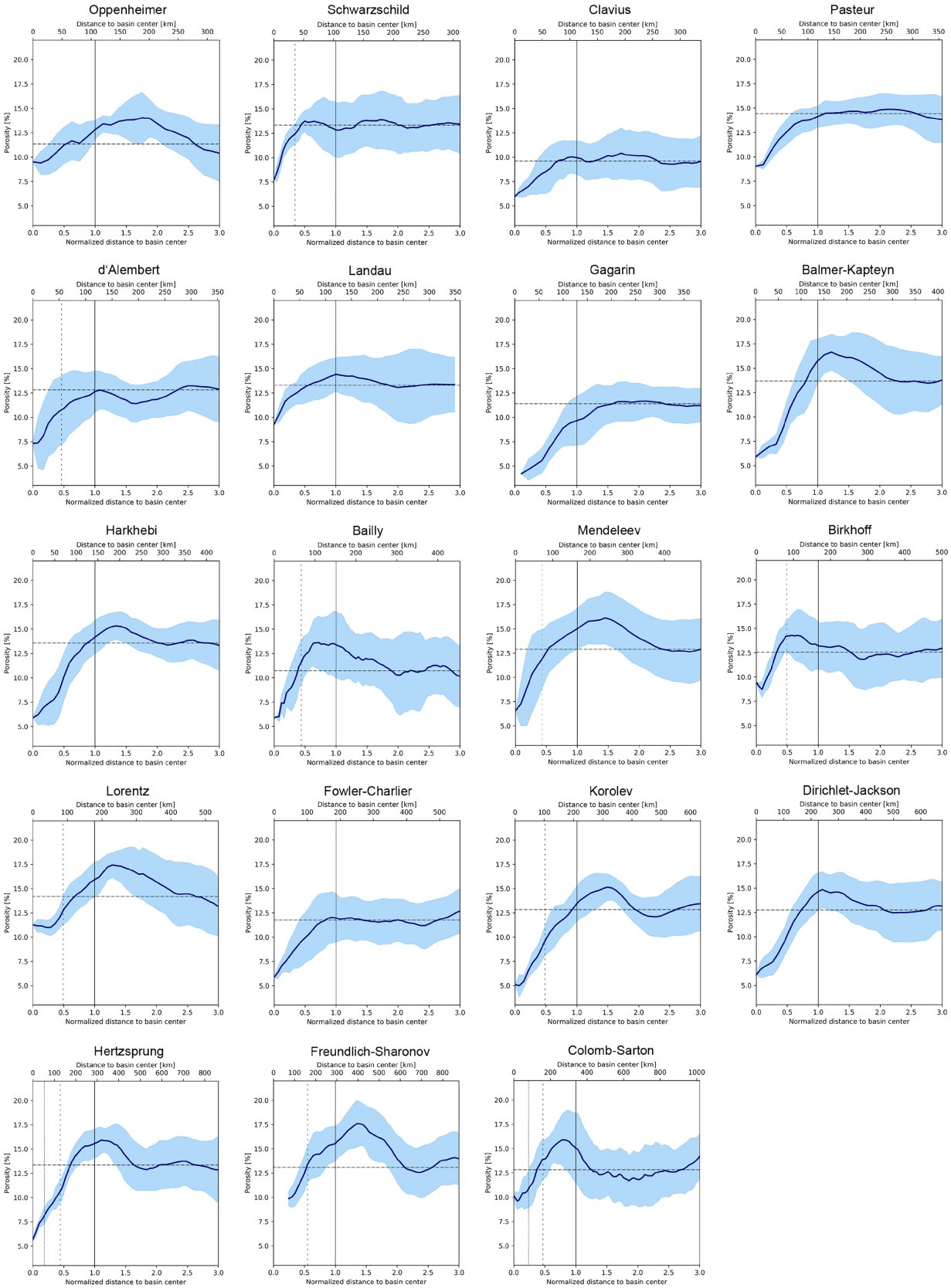


**Figure 5.** Azimuthally averaged radial porosity profiles of impact basins located in the lunar highlands that show a distinct porosity signature. Figure format is the same as in Figure 4.

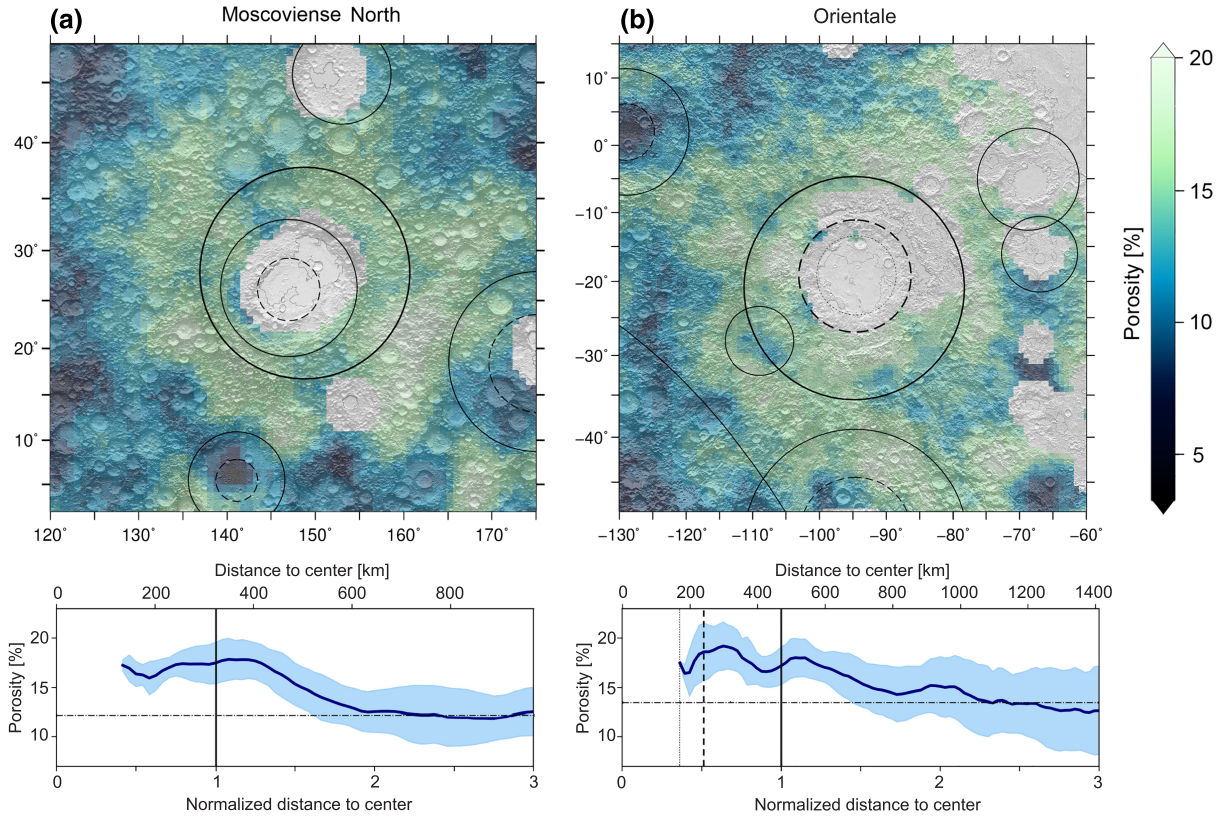


**Figure 6.** Porosity maps of (a) Moscoviense and (b) Orientale basin with shaded-relief Lunar Orbiter Laser Altimeter (LOLA) topography in the background and azimuthally averaged profiles of porosity with their corresponding standard deviations (below). Maps are plotted in a Mercator projection. The image format is the same as in Figure 4.

is Nectarian in age, whereas Orientale is 937 km in diameter and one of the youngest basins with an Imbrian age. Both exhibit very high porosities in their surroundings as shown in Figure 6. Though the porosity could not be determined in the basin interior, as a result of the presence of mare basalts, extremely high porosities are found to extend out to almost 2 crater radii from the basin center. The porosity peaks for Moscoviense and Orientale at 20% and 22%, respectively, which are 8% greater than the ambient porosity.

In Table 1 we list the porosity characteristics of all basins that have been investigated in this study. For each basin we estimated the azimuthally averaged minimum porosity $\phi_{min}$, the azimuthally averaged maximum porosity $\phi_{max}$, and the porosity contrast $\phi_{diff}$, which is defined as the difference between the maximum and minimum porosity. The ambient value of the crustal porosity is also provided, which represents an average between 2 and 3 main rim radii. Basins for which the minimum porosity could not be determined because of the presence of mare in their centers are enclosed by parentheses. The South Pole-Aitken (SPA) basin is not included in the list, since meaningful values cannot be determined, as a result of the huge dimension of the basin and the presence of numerous superposed younger basins. Instead, in the Appendix we provide a detailed map of the South Pole-Aitken basin porosity together with an azimuthally averaged porosity profile (Figure S3). As shown in the table, the minimum porosities vary from 4% to 16%, the maximum porosity ranges from 10% to 19%, and the ambient porosities vary between 10% and 16%. The porosity contrasts vary from 1% to 11%.

## 4. Discussion

### 4.1. Porosity Characteristics of Impact Basins

Many lunar impact basins show marked crustal porosity anomalies that stand out against the global background (Figure 3). These basins all possess a similar signature where the porosity is reduced within the peak ring and the porosity is highest close to and just exterior to the main rim. Other basins have less well characterized profiles, and the most likely explanation for this is that the initial porosity signature was modified by

**Table 1**
*Porosity characteristics of investigated lunar basins*

| Basin name | Diameter[a] [km] | Min. porosity within basin [%] | Standard deviation [%] | Max. porosity [%] | Standard deviation [%] | Porosity contrast [%] | Standard deviation [%] | Ambient porosity [%] |
|---|---|---|---|---|---|---|---|---|
| Wegener-Winlock | 205 | 15.5 | 0.4 | 16.7 | 0.0 | 1.3 | 0.4 | 14.2 |
| Humboldt | 206 | (11.6) | 1.4 | 13.9 | 2.7 | (2.4) | 4.1 | 13.3 |
| Oppenheimer | 206 | (9.4) | 1.2 | 14.0 | 2.6 | (4.6) | 3.8 | 11.3 |
| Schwarzschild | 207 | 7.7 | 0.0 | 13.9 | 3.0 | 6.2 | 3.0 | 13.3 |
| Galois | 210 | 9.6 | 0.0 | 14.0 | 1.1 | 4.4 | 1.6 | 13.1 |
| Keeler West | 218 | 11.1 | 0.0 | 12.5 | 1.6 | 1.4 | 1.6 | 11.2 |
| Clavius | 220 | 6.0 | 0.0 | 10.4 | 2.6 | 4.5 | 2.6 | 9.6 |
| Deslandres | 220 | 10.5 | 1.1 | 11.8 | 0.9 | 1.3 | 2.1 | 10.2 |
| TOPO-13 | 220 | (9.3) | 0.0 | 13.3 | 1.6 | (3.9) | 1.7 | 10.6 |
| Poczobutt | 225 | 15.0 | 0.6 | 17.8 | 1.6 | 2.7 | 2.3 | 14.1 |
| Pasteur | 231 | 9.1 | 0.0 | 14.9 | 1.6 | 5.8 | 1.7 | 14.8 |
| d'Alembert | 232 | 7.3 | 0.0 | 13.2 | 2.5 | 5.9 | 2.5 | 12.8 |
| Landau | 236 | 9.2 | 0.0 | 14.4 | 1.7 | 5.2 | 1.7 | 13.3 |
| Campbell | 237 | (14.0) | 0.3 | 15.4 | 1.4 | (1.4) | 1.7 | 14.1 |
| Fermi | 241 | (14.2) | 0.6 | 15.6 | 1.3 | (1.4) | 1.8 | 13.4 |
| Gagarin | 256 | (4.2) | 0.0 | 11.7 | 1.7 | (7.4) | 1.7 | 11.4 |
| Milne | 264 | 14.2 | 1.4 | 14.8 | 0.5 | 0.6 | 1.9 | 12.5 |
| Balmer-Kapteyn | 265 | 5.9 | 0.0 | 16.7 | 1.8 | 10.7 | 1.8 | 13.8 |
| Orientale-Southwest | 276 | 14.5 | 0.6 | 17.5 | 1.0 | 3.0 | 1.5 | 16.4 |
| Harkhebi | 280 | 5.9 | 0.0 | 15.3 | 1.4 | 9.4 | 1.9 | 13.1 |
| Bailly | 299 | 5.9 | 0.0 | 13.6 | 2.7 | 7.7 | 2.7 | 10.8 |
| Planck | 321 | 9.7 | 1.5 | 12.0 | 2.7 | 2.3 | 4.2 | 11.7 |
| Mendeleev | 331 | 6.6 | 0.0 | 16.1 | 2.7 | 9.6 | 3.0 | 12.7 |
| Birkhoff | 334 | 8.7 | 0.8 | 14.3 | 2.7 | 5.6 | 3.5 | 12.6 |
| Ingenii | 342 | 10.9 | 2.2 | 14.1 | 2.6 | 3.2 | 4.9 | 10.4 |
| Lorentz | 351 | (11.0) | 0.8 | 17.4 | 1.3 | (6.4) | 2.8 | 14.3 |
| Schiller-Zucchius | 361 | (13.5) | 2.4 | 15.0 | 2.1 | (1.5) | 4.5 | 10.9 |
| Fowler-Charlier | 374 | 5.9 | 0.0 | 12.7 | 2.3 | 6.8 | 2.3 | 11.7 |
| Korolev | 417 | 5.0 | 1.1 | 15.2 | 1.4 | 10.2 | 1.9 | 12.8 |
| Moscovience | 421 | (15.6) | 2.1 | 17.7 | 1.8 | (2.1) | 3.9 | 14.5 |
| Mutus-Vlacq | 450 | 8.0 | 1.0 | 13.4 | 3.2 | 5.4 | 4.1 | 12.4 |
| Dirichlet-Jackson | 452 | 6.1 | 0.0 | 14.9 | 1.8 | 8.8 | 1.8 | 12.7 |
| TOPO-22 | 500 | 8.5 | 0.0 | 13.8 | 3.0 | 5.4 | 3.0 | 13.5 |
| Hertzsprung | 571 | 5.6 | 0.0 | 15.9 | 1.3 | 10.3 | 1.7 | 13.2 |
| Freundlich-Sharonov | 582 | (9.9) | 0.7 | 17.6 | 2.4 | (7.7) | 3.3 | 12.9 |
| Fitzgerald-Jackson | 600 | 12.0 | 0.0 | 14.2 | 2.5 | 2.2 | 2.5 | 13.4 |
| Moscoviense North | 640 | (16.0) | 1.7 | 17.9 | 2.1 | (1.9) | 3.8 | 12.2 |
| Mendel-Rydberg | 650 | (13.8) | 2.2 | 16.5 | 2.5 | (2.8) | 4.7 | 13.4 |
| Coulomb-Sarton | 672 | 9.6 | 0.9 | 15.9 | 2.8 | 6.3 | 3.6 | 12.9 |
| Orientale | 937 | (16.4) | 0.9 | 19.2 | 2.4 | (2.8) | 3.3 | 13.5 |

*Note*. Numbers in parentheses lack data in the basin centers as a result of the presence of mare basalts. Basin names are approved by the International Astronomical Union (IAU) or suggested by Neumann et al. (2015). The ambient porosity is the average porosity between 2 and 3 main rim radii from the basin center.
[a]Data from Neumann et al. (2015).

subsequent impact events. We thus suggest that basins form with an initially well defined and characteristic porosity profile, and that as the crater degrades, the profile becomes more muted and less distinct.

In Figure 4 we show the porosity map and profile of Hertzsprung basin (left), which is representative of an unmodified basin that possesses a clear and distinct porosity pattern. In its center a pronounced porosity low can be found. The porosity is reduced to 5% within a radius of 0.6 crater radii compared to the regional value of 13%. This porosity low is confined largely within the peak ring. From about 0.6 to 1.6 crater radii the porosity is higher than the background value and achieves a maximum value of 16% just beyond the main basin rim at 1.2 crater radii. The maximum porosity of 16% is larger than the background value by 3%. Most basins with clear signatures have similar patterns, though the exact crater radii at the various transitions can vary by about half a crater radius.

The reduced porosity within the basin center is probably the result of several factors. One important contribution is likely the production of impact melt. Impact melt sheets, if sufficiently thick, should form with porosities near zero. As suggested by numerical simulations, the volume of melt is mainly related to the dimension of the projectile (Grieve & Cintala, 1992; Pierazzo et al., 1997), but is also dependent on other factors such as the composition and initial temperature of the target material (Pierazzo et al., 1997), and the impact angle (Pierazzo & Melosh, 2000). Cintala and Grieve (1998) proposed a scaling law for estimating the volume of impact melt $V_M$ under terrestrial and lunar conditions as a function of transient crater diameter $D_{tc}$ in the general form

$$V_M = c\, D_{tc}^{d}, \tag{2}$$

where the constants $c$ and $d$ depend on the impactor velocity and composition. Applying values for a chondritic projectile with an impact velocity of 15 km $s^{-1}$ and assuming a linear relationship between the diameter of the transient and the final crater, a basin with the dimension of Hertzsprung ($D$ = 571 km) would have about 60 times more impact melt than a basin with a diameter of only 200 km. Another crucial parameter controlling the amount of generated melt is the initial porosity of the target material before impact. Numerical simulations by Wünnemann et al. (2008) showed that materials with high initial porosity significantly reduce the critical pressure that is required for melting. Consequently, more melt is generated in target materials of high porosity. Vaughan et al. (2013) modeled impact melt production using the example of Orientale basin. The thickest melt sheet (about 14 km) was found to be located in the basin center, with an extent of approximately 0.7 crater radii. This is about the same size as the peak ring and fits well with the extent of the observed porosity minimum of the basins that do not possess younger mare basalts.

As suggested by numerical models, another factor being responsible for the reduced porosity in a basin's interior could be the compaction of the target material, which is the closing of preexisting pore space (e.g., Collins et al., 2011; Wünnemann et al., 2006). In highly porous targets the effect of compaction plays a fundamental role on the postimpact porosity (Housen & Holsapple, 2003). In particular, numerical simulations by Milbury et al. (2015) showed that preimpact porosities of greater than 7% result in positive Bouguer anomalies (indicating reduced porosities).

The increased porosities that are found near to the crater rim are likely the result of several factors, as well. First, during crater formation, target material gets displaced and deformed. Materials that are ballistically excavated reimpact the surface outside of the transient cavity and form an ejecta blanket, which can be of several tens kilometer thick. The ejecta deposits are generally continuous about 1 crater radii away from the rim, beyond which the deposits become discontinuous and thin. The ejecta deposits are expected to have extremely high porosities as a result of the excavation and reimpact processes. Second, as a result of the passing shock wave and the subsequent shear-dominated cratering flow, fracturing and brecciation raise the porosity of the target material (Collins et al., 2004; Pilkington & Grieve, 1992). Dilatancy, which is the increase in volume of a rock while subject to shear deformation, would also contribute to raise the porosity (Collins, 2014). Numerical simulations by Wiggins et al. (2019) showed that the impact of projectiles with sizes of 1 to 10 km (which create craters with diameters of about 10 to 100 km) would create significant fracturing to depths of at least 20 km. Since the porosities estimated in our study represent an average of the upper several kilometers of the lunar crust, we emphasize that it is not possible to distinguish between deep porosity caused by fracturing of the in situ crust by shock waves or by the overlying ejecta blanket that represents ballistically excavated materials.

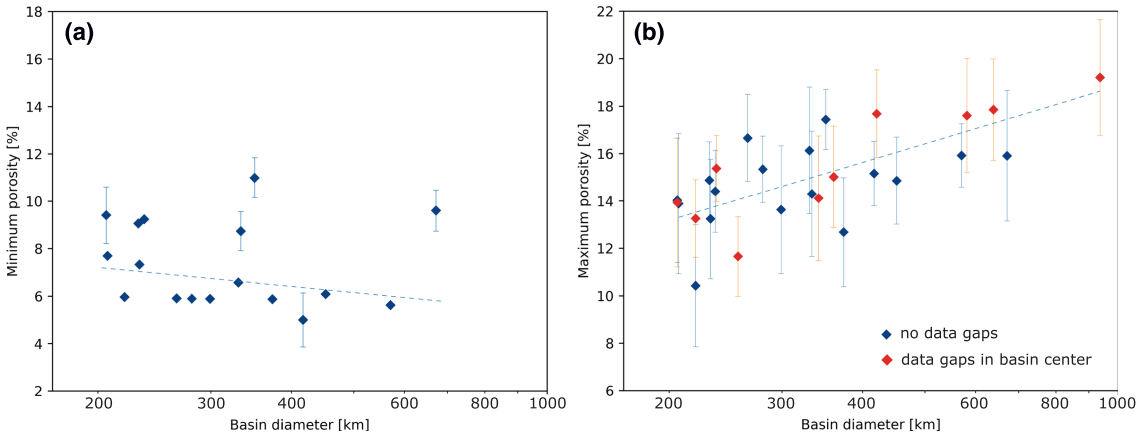


**Figure 7.** (a) Minimum porosity $\phi_{min}$ and (b) maximum porosity $\phi_{max}$ as a function of the main rim diameter (Neumann et al., 2015) for selected pristine basins. Basins which lack data in their center due to of presence of mare basalt are marked in red and were excluded when estimating the trendline for the minimum porosity.

### 4.2. Porosity Structure in Relation to Basin Diameter and Age

The majority of the investigated basins in our study have younger impact basins in their vicinity. These later superposed craters and basins likely interfered with the previously existing porosity structure, leading to substantial lateral variability in the porosity of the superposed impact basin. Of the 40 basins that were investigated, only 27 were likely not disturbed by later large scale impact events (see Figure 5 and S2). The characteristics of these relatively pristine basins are investigated further in Figure 7, where we plot both the minimum and maximum porosity as a function of basin diameter. Those basins that lack density estimates in their interiors as a result of mare basalts are plotted in red.

We first find that the maximum porosity increases with increasing basin diameter, from values close to 13% at 200 km diameter to 18% at 900 km diameter. We explain the increased porosities for larger basins by more material being excavated as the basin increases in size, leading to thicker ejecta blankets of highly porous and fractured material outside the transient crater. Since for larger basins a larger extent of the isobaric core (Pierazzo et al., 1997) is expected (within this region, the peak shock pressure reaches it maximum value), the fracture zone for larger basins should be shifted further outwards. In the left panel of Figure 7 we plot the minimum porosity as a function of crater diameter. For this measure, the basins with data gaps in their center should be considered unreliable, given that the lowest porosities are found generally in the basin center. When excluding those basins, we find that the minimum porosity only slightly decreases with increasing basin size, from about 7% at 200 km diameter to 6% at 600 km diameter. This small effect could be related to the larger quantities and depths of impact melt that are generated by larger basins.

We next investigated how the porosity structure of individual basins varies with respect to their ages (Figure 8). Though some of the basins in our study have well known relative and/or absolute ages, the formation time of many basins are unknown. For the relative ages, we made use of the sequences published in Spudis et al. (2011) and Orgel et al. (2018). For the most part, these are consistent with previous work by Wilhelms (1987). If a relative basin age could not be found, we removed it from the consideration in our analysis.

In Figure 8, we plot both the minimum and maximum porosities of the pristine basins as a function of relative age, where the ages decrease with increasing sequence number. We first find that the minimum porosity in the basin center is smallest for the youngest basins (about 5%), having a model age of about 3.81 Ga, and largest for the oldest basins (about 11%) with an approximate model age of 4.28 Ga (Orgel et al., 2018). We attribute this behavior to older basins being subjected to numerous smaller impact events (meter to kilometer scale), which progressively fractures the impact melt sheet with increasing time. For the oldest basins, the minimum porosity is not too different from the background value far from the basin center. For the maximum porosity shown in the right panel, a slight increase in maximum porosity with decreasing age is observed, from about 15% for the oldest basins to about 16% for the youngest.

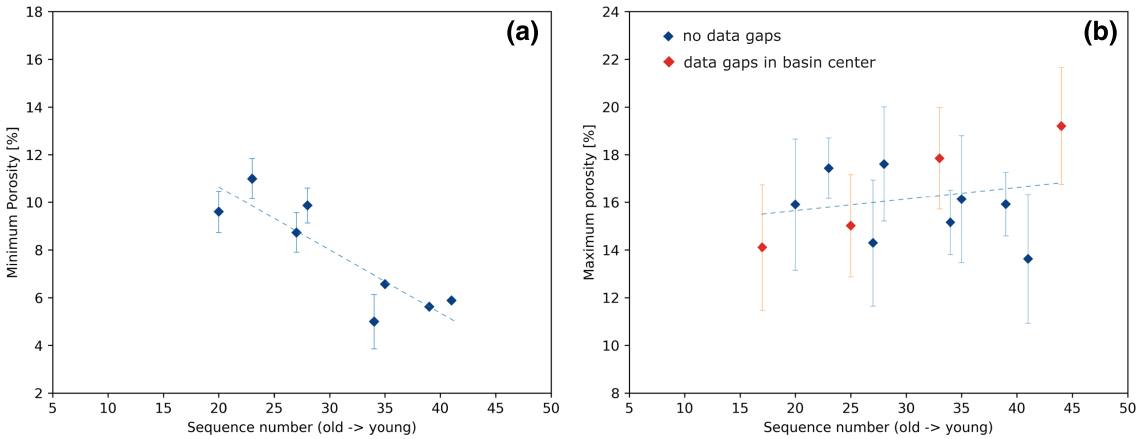


**Figure 8.** (a) Minimum porosity $\phi_{min}$ and (b) maximum porosity $\phi_{max}$ as a function of basin formation sequence (Orgel et al., 2018; Spudis et al., 2011). Basins that lack data in their center due to of presence of mare basalt are marked in red and were excluded when estimating the trendline for the minimum porosity. Basins with unknown relative or absolute ages were omitted from the analysis.

## 5. Summary

High resolution gravity data from recent gravity models of the Moon have allowed us to estimate the bulk density and porosity of the upper lunar crust. The spatial resolution of our bulk density estimates are about a factor of two better than previous studies that used lower resoution gravity data, and this allowed us to investigate the porosity structure of lunar impact basins. We find that the upper crust exhibits a wide range of porosities, with values between 3% and 24%. Our global high-resolution porosity map provides clear evidence that large impact basins both increase and reduce porosity. Many basins show a distinct porosity signature, with low porosities in their center within the peak ring (if one exists), and increased porosities close to and just exterior to the main rim. Other basins show a less distinctive and muted porosity pattern, which are attributed to postimpact modification by superposed large basins and craters. We suggest that after formation all basins show pronounced porosity signature and that basins that have been exposed to subsequent large scale impact events show a modified and more muted porosity pattern. The larger the impact basin, the more pronounced are the minimum and maximum porosities. Furthermore, we demonstrate a correlation between the porosity structure of impact basins and their relative ages. While older candidates show a less pronounced porosity signature with a lower porosity contrast, younger basins show the highest porosities near their rims and the lowest values interior to the peak ring. We relate the lower contrast for older candidates to modifications through later impacts. The results of the present work will help constrain models of impact crater formation that consider both fracturing and compaction of the crust.

**Acknowledgments**
Daniel Wahl was supported by the Deutsche Forschungsgemeinschaft (DFG) Grant SFB-TRR 170, Subproject A04-83. Mark A. Wieczorek was partially supported by a grant from the French space agency (CNES). We gratefully acknowledge Jason Soderblom and an anonymous reviewer for their helpful comments improving the manuscript. The GRAIL gravity model GL1500E as well as topography data LOLA2600p can be accessed online via the NASA Planetary Data System (https://pds.nasa.gov/). All data to reproduce the results and figures in this work can be accessed online (https://doi.org/10.17632/jmd84c6f64.1).

## References

Besserer, J., Nimmo, F., Wieczorek, M. A., Weber, R. C., Kiefer, W. S., McGovern, P. J., et al. (2014). GRAIL gravity constraints on the vertical and lateral density structure of the lunar crust. *Geophysical Research Letters*, *41*, 5771–5777. https://doi.org/10.1002/2014GL060240

Cintala, M. J., & Grieve, R. A. F. (1998). Scaling impact melting and crater dimensions: Implications for the lunar cratering record. *Meteoritics and Planetary Science*, *33*(4), 889–912. https://doi.org/10.1111/j.1945-5100.1998.tb01695.x

Collins, G. S. (2014). Numerical simulations of impact crater formation with dilatancy. *Journal of Geophysical Research: Planets*, *119*, 2600–2619. https://doi.org/10.1002/2014JE004708

Collins, G. S., Melosh, H. J., & Ivanov, B. A. (2004). Modeling damage and deformation in impact simulations. *Meteoritics and Planetary Science*, *39*(2), 217–231. https://doi.org/10.1111/j.1945-5100.2004.tb00337.x

Collins, G. S., Melosh, H. J., & Wünnemann, K. (2011). Improvements to the $\epsilon$-$\alpha$ Porous compaction model for simulating impacts into high-porosity solar system objects. *International Journal of Impact Engineering*, *38*(6), 434–439. https://doi.org/10.1016/j.ijimpeng.2010.10.013

Crameri, F. (2018). Scientific colour-maps. Zenodo. https://doi.org/10.5281/zenodo.1243862

Förstner, U. (1967). Petrographische Untersuchungen des Suevit aus den Bohrungen Deiningen und Wörnitzostheim im Ries von Nördlingen. *Contributions to Mineralogy and Petrology*, *15*(4), 281–308. https://doi.org/10.1007/BF00404198

Gong, S., Wieczorek, M. A., Nimmo, F., Kiefer, W. S., Head, J. W., Huang, C., et al. (2016). Thicknesses of mare basalts on the Moon from gravity and topography. *Journal of Geophysical Research: Planets*, *121*, 854–870. https://doi.org/10.1002/2016JE005008

Grieve, R. A. F., & Cintala, M. J. (1992). An analysis of differential impact melt-erater scaling and implications for the terrestrial impact record. *Meteoritics*, *27*(5), 526–538. https://doi.org/10.1111/j.1945-5100.1992.tb01074.x

Housen, K. R., & Holsapple, K. A. (2003). Impact cratering on porous asteroids. *Icarus*, *163*(1), 102–119. https://doi.org/10.1016/S0019-1035(03)00024-1

Huang, Q., & Wieczorek, M. A. (2012). Density and porosity of the lunar crust from gravity and topography. *Journal of Geophysical Research*, *117*, E05003. https://doi.org/10.1029/2012JE004062

Kiefer, W. S., MacKe, R. J., Britt, D. T., Irving, A. J., & Consolmagno, G. J. (2012). The density and porosity of lunar rocks. *Geophysical Research Letters*, *39*, L07201. https://doi.org/10.1029/2012GL051319

Konopliv, A. S., Park, R. S., Yuan, D.-N., Asmar, S. W., Watkins, M. M., Williams, J. G., et al. (2014). High-resolution lunar gravity fields from the GRAIL Primary and Extended Missions. *Geophysical Research Letters*, *41*, 1452–1458. https://doi.org/10.1002/2013GL059066

Lemoine, F. G., Goossens, S., Sabaka, T. J., Nicholas, J. B., Mazarico, E., Rowlands, D. D., et al. (2014). GRGM900C: A degree 900 lunar gravity model from GRAIL primary and extended mission data. *Geophysical Research Letters*, *41*, 3382–3389. https://doi.org/10.1002/2014GL060027

Love, S. G., Horz, F., & Brownlee, D. E. (1993). Target porosity effects in impact cratering. *Icarus*, *105*, 216–224. https://doi.org/10.1006/icar.1993.1119

Melosh, H. J., Freed, A. M., Johnson, B. C., Blair, D. M., Solomon, S. C., Wieczorek, M. A., & Zuber, M. T. (2013). The origin of lunar mascon basins. *Science*, *340*, 1552–1556. https://doi.org/10.1126/science.1235768

Milbury, C., Johnson, B. C., Melosh, H. J., Collins, G. S., Blair, D. M., Soderblom, J. M., et al. (2015). Preimpact porosity controls the gravity signature of lunar craters. *Geophysical Research Letters*, *42*, 9711–9716. https://doi.org/10.1002/2015GL066198

NASA (2008). A standardized lunar coordinate system for the lunar reconnaissance orbiter and lunar datasets. *LRO Proj. LGCWG White Pap.*, *5*, 13.

Nelson, D. M., Koeber, S. D., Daud, K., Robinson, M. S., Watters, T. R., Banks, M. E., & Williams, N. R. (2014). Mapping lunar maria extents and lobate scarps using LROC image products. LPSC abtract #2861.

Neumann, G. A., Zuber, M. T., Wieczorek, M. A., Head, J. W., Baker, D. M. H., Solomon, S. C., et al. (2015). Lunar impact basins revealed by Gravity Recovery and Interior Laboratory measurements. *Science Advances*, *1*(9), e1500852–e1500852. https://doi.org/10.1126/sciadv.1500852

Orgel, C., Michael, G., Fassett, C. I., van der Bogert, C. H., Riedel, C., Kneissl, T., & Hiesinger, H. (2018). Ancient bombardment of the inner solar system: Reinvestigation of the fingerprints of different impactor populations on the lunar surface. *Journal of Geophysical Research: Planets*, *123*, 748–762. https://doi.org/10.1002/2017JE005451

Park, R. S., Knopoliv, A. S., Yuan, D.-N., Asmar, S., Watkins, M. M., Williams, J., et al. (2015). A high-resolution spherical harmonic degree 1500 lunar gravity field from the GRAIL mission. AGU Fall-Meeting, abstract #G41B-01.

Pierazzo, E., & Melosh, H. J. (2000). Melt production in oblique impacts. *Icarus*, *145*(1), 252–261.

Pierazzo, E., Vickery, A. M., & Melosh, H. J. (1997). A reevaluation of impact melt production. *Icarus*, *127*, 408–423. https://doi.org/10.1006/icar.1999.6332

Pilkington, M., & Grieve, R. A. F. (1992). The geophysical signature of terrestrial impact craters (1992).pdf. *Reviews of Geophysic*, *30*, 161–181. https://doi.org/10.1006/icar.1997.5713

Pohl, J., Stöffler, D., Gall, H., & Ernstson, K. (1977). The Ries impact crater. In D. J. Roddy, R. O. Pepin, & R. B. Merrill (Eds.), *Impact and explosion cratering* (pp. 343–404). New York: Pergamon Press.

Rae, AuriolS. P., Collins, G. S., Morgan, J. V., Salge, T., Christeson, G. L., Leung, J., et al. (2019). Impact induced porosity and microfracturing at the Chicxulub impact structure. *Journal of Geophysical Research: Planets*, *124*, 1960–1978. https://doi.org/10.1029/2019JE005929

Smith, D. E., Zuber, M. T., Neumann, G. A., Mazarico, E., Lemoine, F. G., Head, J. W., et al. (2017). Summary of the results from the lunar orbiter laser altimeter after seven years in lunar orbit. *Icarus*, *283*, 70–91. https://doi.org/10.1016/j.icarus.2016.06.006

Soderblom, J. M., Evans, A. J., Johnson, B. C., Melosh, H. J., Miljkovi, K., Phillips, R. J., et al. (2015). The fractured Moon: Production and saturation of porosity in the lunar highlands from impact cratering. *Journal of Geophysical Research: Planets*, *42*, 6939–6944. https://doi.org/10.1002/2015GL065022

Spudis, P. D., Wilhelms, D. E., & Robinson, M. S. (2011). The Sculptured Hills of the Taurus Highlands: Implications for the relative age of Serenitatis, basin chronologies and the cratering history of the Moon. *Journal of Geophysical Research*, *116*, E00H03. https://doi.org/10.1029/2011JE003903

Vaughan, W. M., Head, J. W., Wilson, L., & Hess, P. C. (2013). Geology and petrology of enormous volumes of impact melt on the Moon: A case study of the Orientale basin impact melt sea. *Icarus*, *223*(2), 749–765. https://doi.org/10.1016/j.icarus.2013.01.017

Wahl, D., & Oberst, J. (2019). Lateral variations in bulk density and porosity of the upper lunar crust from high-resolution gravity and topography data: Comparison of different analysis techniques. *ISPRS Annals of the Photogrammetry, Remote Sensing and Spatial Information Sciences*, *4*, 527–532. https://doi.org/10.5194/isprs-annals-IV-2-W5-527-2019

Warren, P. H. (2001). Porosities of lunar meteorites: Strength, porosity, and petrologic screening during the meteorite delivery process. *Journal of Geophysical Research*, *106*(E5), 10,101–10,111. https://doi.org/10.1029/2000JE001283

Wieczorek, M. A. (2015). Gravity and topography of the terrestrial planets, (2nd). In G. Schubert & T. Spohn (Eds.), *Treatise on geophysics: Planets and Moons* (Vol. 10, pp. 153–193): Elsevier. https://doi.org/10.1016/B978-0-444-53802-4.00169-X

Wieczorek, M. A., & Meschede, M. (2018). SHTools: Tools for working with spherical harmonics. *Geochemistry, Geophysics, Geosystems*, *19*, 2574–2592. https://doi.org/10.1029/2018GC007529

Wieczorek, M. A., Neumann, G. A., Nimmo, F., Kiefer, W. S., Taylor, J. G., Melosh, H. J., et al. (2013). The crust of the Moon as Seen by GRAIL. *Science*, *339*, 671–675. https://doi.org/10.1126/science.1231530

Wieczorek, M. A., & Phillips, R. J. (1998). Potential anomalies on a sphere: Applications to the thickness of the lunar crust. *Journal of Geophysical Research*, *103*(97), 1715–1724. https://doi.org/10.1029/97JE03136

Wiggins, S. E., Johnson, B. C., Bowling, T. J., Melosh, H. J., & Silber, E. A. (2019). Impact fragmentation and the development of the deep lunar megaregolith. *Journal of Geophysical Research: Planets*, *124*, 941–957. https://doi.org/10.1029/2018JE005757

Wilhelms, D. E. (1987). The geologic history of the moon. ISGS Numbered Series, No. 1348. https://doi.org/10.3133/pp1348

Wünnemann, K., Collins, G. S., & Melosh, H. J. (2006). A strain-based porosity model for use in hydrocode simulations of impacts and implications for transient crater growth in porous targets. *Icarus*, *180*(2), 514–527. https://doi.org/10.1016/j.icarus.2005.10.013

Wünnemann, K., Collins, G. S., & Osinski, G. R. (2008). Numerical modelling of impact melt production in porous rocks. *Earth and Planetary Science Letters*, *269*, 530–539. https://doi.org/10.1016/j.epsl.2008.03.007

Zuber, M. T., Smith, D. E., Watkins, M. M., Asmar, S. W., Konopliv, A. S., Lemoine, F. G., et al. (2013a). Gravity field of the Moon from the Gravity Recovery and Interior Laboratory (GRAIL) mission. *Science*, *339*, 2011–2014. https://doi.org/10.1126/science.1231507